



# P- and S-wave velocity structure of central West Antarctica: Implications for the tectonic evolution of the West Antarctic Rift System



Erica M. Lucas <sup>a,\*</sup>, David Soto <sup>a</sup>, Andrew A. Nyblade <sup>a</sup>, Andrew J. Lloyd <sup>b</sup>, Richard C. Aster <sup>c</sup>, Douglas A. Wiens <sup>b</sup>, John Paul O'Donnell <sup>d</sup>, Graham W. Stuart <sup>d</sup>, Terry J. Wilson <sup>e</sup>, Ian W. Dalziel <sup>f</sup>, J. Paul Winberry <sup>g</sup>, Audrey D. Huerta <sup>g</sup>

<sup>a</sup> Department of Geosciences, Pennsylvania State University, 503 Deike Building, University Park, PA 16802, United States of America

<sup>b</sup> Department of Earth and Planetary Sciences, Washington University in St. Louis, 1 Brookings Dr., St. Louis, MO 63130, United States of America

<sup>c</sup> Department of Geosciences, Warner College of Natural Resources, Colorado State University, 400 University Ave., Fort Collins, CO 80523, United States of America

<sup>d</sup> School of Earth and Environment, University of Leeds, Leeds LS2 9JT, United Kingdom

<sup>e</sup> School of Earth Sciences, Ohio State University, 125 Oval Dr. S, Columbus, OH 43210, United States of America

<sup>f</sup> Jackson School of Geosciences, University of Texas at Austin, 2305 Speedway, Austin, TX 78712, United States of America

<sup>g</sup> Department of Geological Sciences, Central Washington University, 400 E. University Way, Ellensburg, WA 98926, United States of America

## ARTICLE INFO

### Article history:

Received 14 January 2020

Received in revised form 2 June 2020

Accepted 22 June 2020

Available online 3 July 2020

Editor: M. Ishii

### Keywords:

Antarctica

West Antarctic Rift System

mantle structure

seismic tomography

West Antarctic Ice Sheet

## ABSTRACT

New P- and S-wave velocity models of the upper mantle from 100 to 400 km depth beneath the central portions of West Antarctica, obtained by inverting relative travel-times from teleseismic earthquakes recorded on Polar Earth Observing Network (POLENET/ANET) and UK Antarctic Network (UKANET) seismic stations between 2007 and 2017, reveal a heterogeneous upper mantle. A low velocity anomaly ( $-1.0\% V_p$ ;  $-2.0\% V_s$ ) imaged beneath Marie Byrd Land is attributed to thermally perturbed upper mantle of possible plume origin, and a low velocity anomaly imaged beneath the Pine Island Glacier and the mouth of Thwaites Glacier is interpreted as a rift-related thermal structure that may include warm mantle flowing from Marie Byrd Land. High velocity anomalies ( $\leq 0.8\% V_p$ ;  $1.5\% V_s$ ) imaged in the central portion of the West Antarctic Rift System indicate the presence of lithosphere unmodified by tectonic activity since the Late Cretaceous formation of the rift system. Within the region of high velocities, localized low velocity anomalies beneath parts of the Bentley Subglacial Trench are suggestive of focused Cenozoic rifting. The models also show variable velocity structure beneath the Haag-Ellsworth Whitmore crustal block and low velocities beneath the Thurston Island-Eights Coast crustal block. The heterogeneous upper mantle structure of central West Antarctica indicates that upper mantle temperatures could vary by 100 K or more over distances of less than 100 km, which may add complexity to solid earth-ice interactions and influence basal ice sheet conditions.

© 2020 Elsevier B.V. All rights reserved.

## 1. Introduction

Understanding the structure and tectonic history of the West Antarctic Rift System (WARS; Fig. 1), a first-order tectonic feature of the Antarctic plate, is not only important for advancing our

knowledge of Antarctic geology but also for modeling solid earth-ice interactions in West Antarctica. The tectonic evolution of the WARS has been long debated because of uncertainty in how much of the present-day rift morphology and structure resulted from Mesozoic rifting versus Cenozoic to recent extension (e.g., Dalziel and Elliot, 1982; Fitzgerald, 2002; Siddoway, 2008; Jordan et al., 2010; Granot et al., 2013; Harry et al., 2018; O'Donnell et al., 2019; Lloyd et al., 2019). Because much of the WARS lies within central West Antarctica, improved seismic velocity models of upper mantle structure beneath central West Antarctic are critical for developing a more complete understanding of the WARS and unraveling its tectonic history.

\* Corresponding author.

E-mail addresses: emlucas@psu.edu (E.M. Lucas), david\_soto\_73@yahoo.com (D. Soto), aan2@psu.edu (A.A. Nyblade), lloyd42486@gmail.com (A.J. Lloyd), rick.aster@colostate.edu (R.C. Aster), doug@wustl.edu (D.A. Wiens), johnpaulodonnel@gmail.com (J.P. O'Donnell), g.w.stuart@leeds.ac.uk (G.W. Stuart), wilson.43osu@gmail.com (T.J. Wilson), ian@ig.utexas.edu (I.W. Dalziel), paul.winberry@gmail.com (J.P. Winberry), huertaa@geology.cwu.edu (A.D. Huerta).

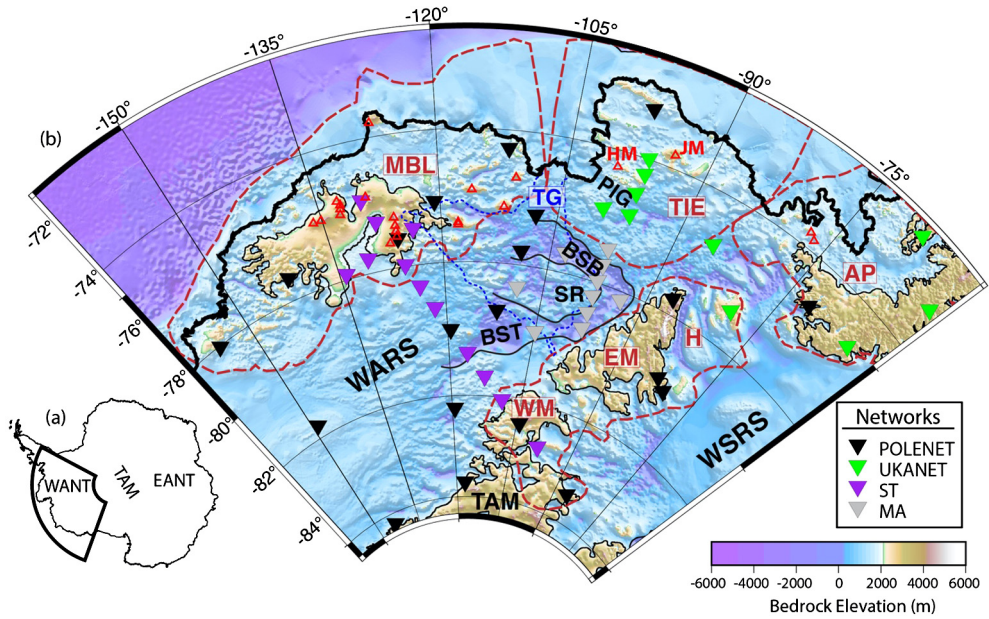


**Fig. 1.** (a) Map of Antarctica with location of study region outlined in bold black line. WANT: West Antarctica, TAM: Transantarctic Mountains, EANT: East Antarctica. (b) Seismic stations used in this study plotted on BEDMAP2 bedrock topography (Fretwell et al., 2013). Dark red dashed lines delineate major crustal blocks (Dalziel and Elliot, 1982), including MBL: Marie Byrd Land, H-EM-WM: Haag-Ellsworth Whitmore, hereafter HEW, TIE: Thurston Island-Eights Coast, AP: Antarctic Peninsula. The Byrd Subglacial Basin (BSB) and Bentley Subglacial Trench (BST) are outlined in black. The Thwaites Glacier catchment is outlined in blue dashed line. The thin, solid black lines contour the 2000 m bedrock elevation. Red triangles mark the locations of known subaerial Cenozoic volcanoes (LeMasurier and Thomson, 1990). Other abbreviated geographic features: WARS: West Antarctic Rift System, SR: Sinuous Ridge, PIG: Pine Island Glacier, WSRS: Weddell Sea Rift System, JM: Jones Mountains; HM: Hudson Mountains. (For interpretation of the colors in the figure(s), the reader is referred to the web version of this article.)

Improved seismic velocity models, which provide important constraints on mantle viscosity and heat flow, are also needed to further progress investigations of solid earth-ice interactions in central West Antarctica. Central West Antarctica contains much of the West Antarctic Ice Sheet, including Thwaites Glacier and Pine Island Glacier, the largest contributors to ice mass loss and sea level rise in Antarctica (e.g., Shepherd et al., 2019) (Fig. 1). Recent studies have shown that projections of Thwaites Glacier and other glaciers in Antarctica require constraints on Earth properties at and below the ice-bed interface (e.g., Barletta et al., 2018). In addition to many cryospheric and climatic processes, ice-sheet stability is strongly influenced by isostatic rebound of the solid Earth in response to past mass loss (e.g., Pattyn and Morlighem, 2020). The spatial rebound patterns and rates, in turn, critically depend on mantle viscosity, which is poorly known in Antarctica (e.g., Powell et al., 2019). Heterogeneity in Earth properties also likely correlates with the distribution of important, but largely uncharacterized, influences on ice-sheet basal lubrication, such as heat flow (e.g., Seroussi et al., 2017). The relevance of seismic images for coupled earth-ice modeling in Antarctica is well illustrated by White-Gaynor et al. (2019), whose images of variations in upper mantle structure beneath the western portions of West Antarctica indicate  $\geq 10 \text{ mWm}^{-2}$  and  $10^2 \text{ Pa s}$  changes in heat flow and mantle viscosity, respectively, over distances of a few hundred kilometers or less.

In this paper, we present new P- and S-wave velocity models of the upper mantle beneath the central portion of West Antarctica that geographically complement the White-Gaynor et al. (2019) models and improve on previous body wave tomography models of West Antarctica (e.g., Hansen et al., 2014; Lloyd et al., 2015), which did not have access to the expanded seismic dataset used in this study. This study also complements several surface wave tomography studies of West Antarctica (Heeszel et al., 2016; Shen et al., 2018; O'Donnell et al., 2019), which have diminished spatial resolution of structure in the 100–400 km depth range compared to this study. In addition to providing new insights into the na-

ture of the upper mantle beneath central West Antarctica and the tectonic evolution of the WARS, our P- and S-wave models provide new constraints on mantle structure needed for coupled solid earth-ice modeling.

## 2. Tectonic history and geology

Antarctica is divided by the  $\sim 3500$  km-long Transantarctic Mountains (Fitzgerald, 2002) into East Antarctica, a large Precambrian shield, and West Antarctica (WANT) (Fig. 1a). WANT is composed of four discrete crustal blocks, separated by the WARS (e.g., Dalziel and Elliot, 1982; Torsvik et al., 2008) (Fig. 1b). The crustal blocks of WANT include: the Antarctic Peninsula (AP), Marie Byrd Land (MBL), the Thurston Island-Eights Coast (TIE) block, and the Haag-Ellsworth Whitmore (HEW) block (Fig. 1b). While the AP, MBL, and the TIE block are all fore-arc and magmatic-arc terranes that developed along the paleo-Pacific subduction margin of Gondwana (e.g., Dalziel, 1992), the HEW block is considered an allochthonous continental fragment (e.g., Jordan et al., 2017). Pine Island Glacier (PIG) and Thwaites Glacier (TG), located along the Amundsen Sea Embayment (ASE) (Fig. 1b), are the fastest flowing and most rapidly retreating glaciers in the West Antarctic Ice Sheet (e.g., Shepherd et al., 2019). PIG lies entirely within the TIE crustal block, while TG sits at the junction of the WARS, MBL, and the TIE.

### 2.1. West Antarctic Rift System

The WARS, a region of thinned, subsided continental crust, extends from the Ross Sea to the Weddell Sea and is bound by MBL and TIE to the north and the Transantarctic Mountains to the south (Fig. 1b). Driven by the waning subduction of the Phoenix plate, the major WARS extensional phase occurred between  $\sim 105$ – $85$  Ma when WANT transitioned from a compressional to an extensional tectonic regime (e.g., Siddoway, 2008). Extension in the WARS continued until the initiation of sea-floor spreading as Zealandia detached from WANT  $\sim 84$  Ma (e.g., Siddoway, 2008).

In comparison to the surrounding regions, crustal thickness within the WARS is relatively thin, ranging from 19 km to 29 km (e.g., Chaput et al., 2014; Ramirez et al., 2016, 2017; Shen et al., 2018). Based on GPS measurements and minimal tectonic seismicity, it is unlikely that the WARS is actively extending (e.g., Winberry and Anandakrishnan, 2003). GPS stations deployed on nunataks throughout WANT and the Transantarctic Mountains show no resolvable horizontal motion (Donnellan and Luyendyk, 2004; Wilson et al., 2015), although the GPS data do show that the ASE is undergoing rapid bedrock uplift (41 mm/year) in response to ice mass loss (Barletta et al., 2018). To explain the GPS data, Barletta et al. (2018) argued that the ASE is underlain by low viscosity upper mantle ( $4 \times 10^{18}$  Pascal-second) beneath a thin ( $\leq 60$  km thick) lithosphere.

While there has been much speculation about the origin of deep subglacial basins in the WARS, in particular the Byrd Subglacial Basin (BSB) and Bentley Subglacial Trench (BST), bedrock topography, gravity, magnetic, seismic, crustal thickness, and geo-dynamic modeling studies have been used to support the idea that these features may be Cenozoic rift basins (e.g., Jordan et al., 2010; Chaput et al., 2014; Lloyd et al., 2015; Harry et al., 2018). Granot et al. (2013) suggested that the BSB and BST represent Eocene-Oligocene transcurrent faults that have been reactivated by mid-Miocene to recent extension. Estimates of azimuthal anisotropy in the WARS upper mantle from shear-wave splitting measurements can also be attributed to Neogene extension (Accardo et al., 2014).

## 2.2. Marie Byrd Land

MBL, located north of the WARS between the Amundsen Sea and Ross Sea, is an uplifted region characterized by widespread Cenozoic volcanism (Fig. 1b). MBL is widely underlain by crust that is  $\sim 5$ – $10$  km thicker than beneath the WARS (e.g., Shen et al., 2018). MBL underwent a maximum of  $\sim 3$  km of tectonic uplift, associated with alkaline volcanism, beginning  $\sim 28$ – $30$  Ma, which resulted in the development of a volcanic province including 18 large shield volcanoes (LeMasurier and Landis, 1996). There is evidence of Pliocene volcanism in MBL (Wilch et al., 1999), and subglacial seismicity has been attributed to ongoing magmatism at three locations (Winberry and Anandakrishnan, 2003; Lough et al., 2013).

The source of volcanism in MBL is highly debated. Studies have attributed the volcanism to a shift from subduction-related to rift-related magmatism during the subduction of the Pacific-Phoenix spreading center along the continental margin (Weaver et al., 1994). Alternatively, many studies argue that a mantle plume is feeding the Cenozoic volcanism, resulting in uplift, and some igneous rocks from MBL are thought to have a geochemical plume composition (e.g., Weaver et al., 1994; LeMasurier and Landis, 1996; Panter et al., 1997). Seismic studies have imaged a deep low velocity anomaly beneath MBL that can be attributed to a mantle plume (e.g., Danesi and Morelli, 2001; Hansen et al., 2014; Emry et al., 2015; Lloyd et al., 2015; Heeszel et al., 2016; Shen et al., 2018; O'Donnell et al., 2019; Lloyd et al., 2019), and shear-wave splitting patterns in WANT are consistent with mantle flow from a plume beneath MBL (Accardo et al., 2014).

## 2.3. Thurston Island-Eights Coast crustal block

The TIE block, encompassing Thurston Island, associated minor islands, and the adjacent Eights Coast, is situated between the AP and MBL (Dalziel and Elliot, 1982). In an aerogravity study, Jordan et al. (2010) found evidence for Cenozoic mafic intrusions and narrow-mode rifting beneath PIG. Two Neogene volcanic fields, the Hudson Mountains and the Jones Mountains, are located in the TIE (Fig. 1) (Rowley et al., 1990). The Hudson Mountains are characterized by three large extensively eroded stratovolcanoes (Rowley

et al., 1990). While no primary volcanic landforms remain in the Jones Mountains, Miocene volcanic sequences are widely exposed (Rowley et al., 1990). Using airborne radar data, Corr and Vaughan (2008) also found evidence of a recent ( $207$  BCE  $\pm 240$  years) volcanic eruption in the Hudson Mountains.

Similar to the BST and BSB, the Pine Island Rift may have originated as an Eocene-Oligocene transcurrent fault that underwent mid-Miocene to recent extension (Granot et al., 2013). While Neogene volcanism has been attributed to extension in the TIE block (e.g., Jordan et al., 2010), it may also arise from flow of the MBL mantle plume beneath the TIE block (Hole and LeMasurier, 1994). Support for the plume hypothesis comes from shear-wave splitting measurements (Accardo et al., 2014) and other seismic models of the upper mantle (e.g., Lloyd et al., 2019).

## 2.4. Haag-Ellsworth Whitmore crustal block

The HEW composite crustal block is located south of the Weddell Sea Rift System (Fig. 1b). The HEW block is a geologically and geophysically distinct crustal block within WANT, exhibiting an anomalous stratigraphy and deformational history (Curtis, 2001). The HEW block can be subdivided into the Haag province and the Ellsworth Whitmore Mountains province, which includes the Ellsworth Mountains and adjacent Whitmore Mountains. The HEW has thicker crust in comparison to surrounding crustal blocks, ranging from 30–40 km (Chaput et al., 2014; An et al., 2015; Ramirez et al., 2016, 2017; Shen et al., 2018). Within the HEW block, the Ellsworth Mountains sit on thicker crust ( $\sim 37$  km) compared to both the Whitmore Mountains ( $\sim 30$ – $33$  km) and Haag province ( $\sim 29$  km) (e.g., O'Donnell et al., 2019). Based on aeromagnetic signatures, Jordan et al. (2017) argued that the Haag province and Ellsworth Whitmore Mountains province can be differentiated by their respective basement rock responses to Jurassic extension in the adjacent Weddell Sea Rift System.

## 3. Previous seismological studies

Early continental-scale tomographic studies, constrained by only a few seismic stations, imaged an overall high-velocity upper mantle beneath Antarctica (e.g., Roult et al., 1994). The following generation of continental-scale surface wave studies imaged higher velocities beneath East Antarctica and lower velocities beneath WANT (e.g., Danesi and Morelli, 2001; Ritzwoller et al., 2001), improving model resolution with data from additional seismic stations in Antarctica. Until a significant increase of seismic network coverage in the 2000's, regional-scale geophysical studies in Antarctica were mainly limited to marine, magnetotelluric, and aerogeophysical surveys (e.g., Behrendt et al., 1996; Wannamaker et al., 1996). Many of these early regional scale geophysical studies found evidence of heterogeneity in the upper mantle and crust of WANT that had not been observed in early continental-scale tomography studies.

Seismic coverage in WANT has greatly increased over the past two decades with the development of the Antarctic portion of the Polar Earth Observing Network (POLENET/ANET). The improved seismic coverage has enabled regional-scale studies using body and surface waves, which have greatly improved our understanding of crustal and upper mantle structure in WANT. Upper mantle structure beneath WANT has been investigated in a number of studies using body waves. Hansen et al. (2014) used adaptively parameterized tomography to produce a continental-scale P-wave velocity model that imaged a deep ( $\sim 800$  km), low velocity anomaly beneath MBL, consistent with the presence of a mantle plume. Using P-wave receiver functions, Emry et al. (2015) determined that the upper mantle thermal anomaly beneath MBL does not extend as deep as the mantle transition zone. With improved data coverage

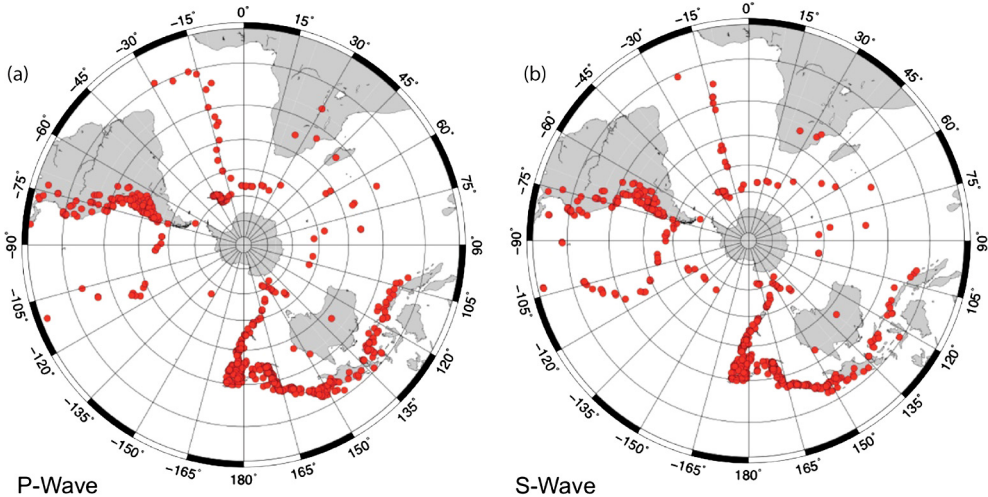


**Fig. 2.** Locations of  $M_b \geq 5.0$  earthquakes (red circles) used in the (a) P-wave and (b) S-wave tomography models.

from the RIS (Mantle Structure and Dynamics of the Ross Sea from a Passive Seismic Deployment on the Ross Ice Shelf) and DRIS (Dynamic Response of the Ross Ice Shelf to Wave-Induced Vibrations) projects. White-Gaynor et al. (2019) imaged lower velocities in the upper mantle beneath MBL and the western portions of the Ross Sea Embayment (RSE) and higher velocities beneath the eastern portion of the Ross Ice Shelf.

Lloyd et al. (2015) used P- and S-wave teleseismic travel times to image upper mantle structure beneath a linear seismic transect (ST) from central MBL to the southern extent of the HEW crustal block. Based on higher velocities imaged throughout most of the WARS, Lloyd et al. (2015) argued that structure in the WARS is mainly dominated by Late Cretaceous/early Cenozoic extension. Aside from higher velocities in the WARS, Lloyd et al. (2015) imaged lower velocities beneath the Bentley Subglacial Trench.

Heeszel et al. (2016) and O'Donnell et al. (2019) used Rayleigh wave tomography to image the upper mantle structure of West Antarctica; in a related study, Shen et al. (2018) jointly inverted Rayleigh wave phase and group velocities along with P-wave receiver functions to image upper mantle structure. All three studies identified anomalously low-velocity upper mantle structure beneath MBL that extends eastward to the Pine Island Bay and beneath parts of TG. They also imaged low-velocity upper mantle structure beneath the HEW block and high-velocity upper mantle structure beneath sections of the WARS. O'Donnell et al. (2019) investigated 3D shear wave velocity structure and anisotropy variations across WANT using surface waves extracted from ambient noise. O'Donnell et al. (2019) imaged high velocity anomalies throughout most of the WARS, a low velocity anomaly beneath the BST, and a low velocity anomaly extending from the MBL dome toward Pine Island Bay, underlying TG but not PIG. Lloyd et al. (2019) used full-waveform adjoint tomography to produce a continental-scale model of the upper mantle and transition zone beneath Antarctica. At shallow depths, Lloyd et al. (2019) imaged low velocities extending east from MBL through the ASE to the AP and deeper low velocity anomalies extending into the transition zone beneath MBL. Aside from the low velocity anomalies in MBL and the coastal regions, Lloyd et al. (2019) imaged near-average mantle velocities throughout much of WANT.

#### 4. Data selection, relative arrival-time calculation

This study utilizes broadband seismic data collected by the Antarctic portion of the Polar Earth Observing Network (POLENET/ANET; [https://doi.org/10.7914/SN/YT\\_2007](https://doi.org/10.7914/SN/YT_2007)) and the UK Antarctic Network (UKANET; [https://doi.org/10.7914/SN/1D\\_2016](https://doi.org/10.7914/SN/1D_2016)) (Fig. 1b).

We used data from 22 POLENET backbone stations, 24 POLENET temporary array stations, and 10 UKANET temporary array stations. The seismic transect array (ST) was deployed across the WARS from Mount Sidley in MBL to the Whitmore Mountains. The seismic transect array consisted of 3 POLENET backbone stations and 14 temporary stations, deployed from 2010–2011, spaced roughly 90 km apart. The seismic mini array (MA) extended from the BSB to the Amundsen Sea and consisted of 10 POLENET stations deployed from 2015–2016 and 10 UKANET stations deployed from 2016–2017. Stations in the mini array were spaced roughly 70 km apart.

Relative arrival times were determined using the multichannel cross-correlation (MCCC) method of VanDecar and Crosson (1990) on body wave arrivals from  $M_b \geq 5.0$  teleseismic earthquakes with epicentral distances ranging from 30° to 90°. We manually picked initial P-wave arrivals on vertical component waveforms after applying a 0.5–2 Hz bandpass Butterworth filter; 11,117 P-wave arrivals were picked from 725 events. Initial S-wave arrivals were picked on transverse component waveforms after applying a 0.04–2 Hz bandpass Butterworth filter; 7,158 S-wave arrivals were picked from 611 events. The azimuthal distribution of events for both the P- and S-wave models is fairly good, with most of the events originating from the South American subduction zones, western Pacific subduction zones, and mid-ocean ridges (Fig. 2).

After manually picking initial arrivals, we used the MCCC approach to determine more precise relative arrival times for events with picks on four or more stations. The MCCC technique consists of (1) cross-correlating all possible trace combinations for each event to find the correlation maxima, (2) determining the best-fitting mean arrival time on each trace using a regularized least-squares optimization, and (3) calculating data error. The cross-correlation is performed on a windowed portion of each trace around the picked phase arrival. Window lengths of 3 and 12 seconds were used for the P and S phases, respectively. The MCCC technique produces accurate arrival time estimates, with standard errors of ~0.04 s and 0.1 s for P- and S-waves, respectively.

#### 5. Inversion of travel-time residuals

The relative travel-time residuals were inverted for a 3-D mantle velocity model using the VanDecar (1991) method. The model parameterization consisted of 21 knots in latitude between  $-68^\circ$  and  $-88^\circ$ , 53 knots in longitude between  $-56^\circ$  and  $-160^\circ$ , and 34 knots extending from the surface to 1600 km depth, for a total of 37,842 knots (Supp. Fig. 1). Throughout the entire model domain, knots were spaced at intervals of  $1^\circ$  in latitude and  $2^\circ$

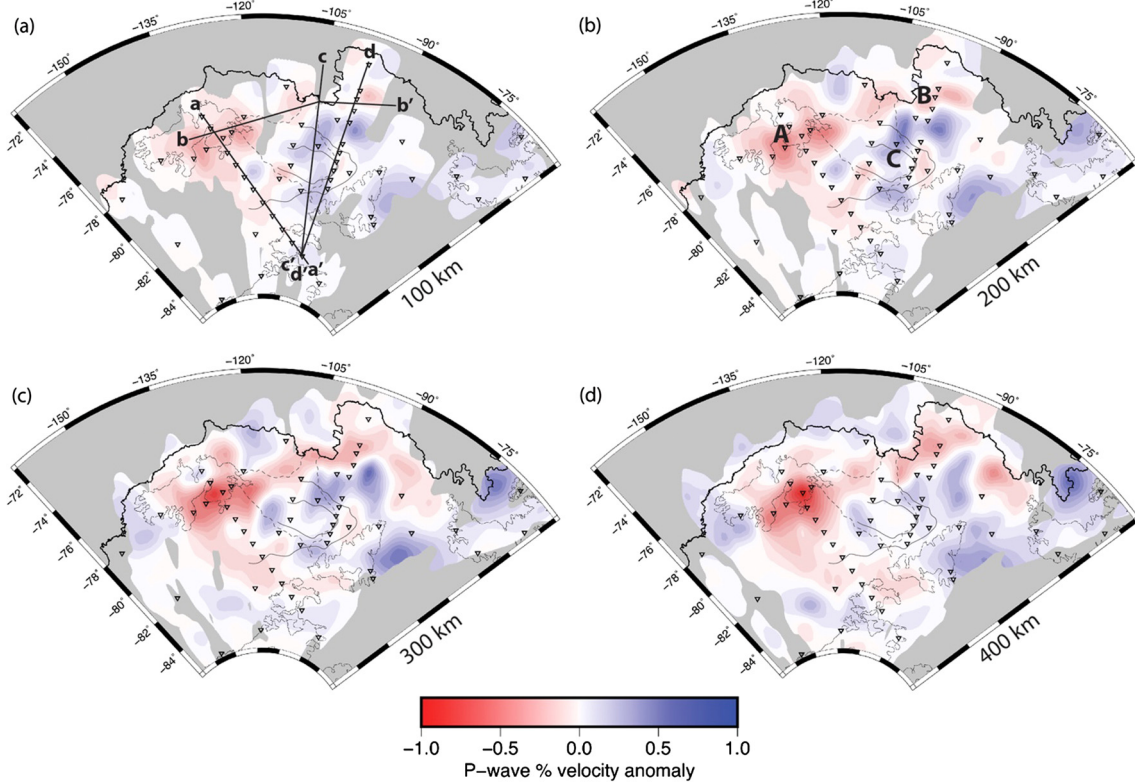


**Fig. 3.** a-d) Depth slices through the P-wave model at 100 km increments. Station locations are marked with triangles. Black lines segments in (a) delineate cross-section locations (a-a', b-b', c-c', d-d'), shown in Fig. 5. The thin, solid black lines contour the 2000 m bedrock elevation. Anomalies A-C, labeled in (b), are discussed in the text.

in longitude with variable knot spacing at depth (Supp. Fig. 1). The grid was designed to overextend the area of interest to avoid mapping unrelated or anomalous structure into the interior of the model.

In the VanDecar method, travel-time residuals are simultaneously inverted for slowness perturbations, station terms, and event relocation terms using a conjugate-gradient algorithm. The station terms account for shallow heterogenous structure at depths that lack crossing ray paths (i.e., <50 km), while travel-time anomalies resulting from event location error and heterogenous structure outside the model domain are absorbed by event relocation terms. The inversion was run through multiple iterations until changes in the model resulted in insignificant changes to the root-mean square (RMS) travel-time residual. Trade-off curves between the RMS travel-time residual and the model roughness were used to determine smoothing and flattening parameters that yielded a model which fit the data with a minimum amount of structure (Supp. Fig. 2). Because the VanDecar method uses relative arrival-times, the inversion method gives velocity perturbations with respect to an unresolved model mean; therefore, absolute velocities cannot be recovered.

## 6. Results

The tomographic models show P-wave velocity perturbations of  $\pm 1.0\%$  and S-wave velocity perturbations of  $\pm 2.0\%$  (Figs. 3, 4, 5). The P- and S-wave models have comparable first-order structures and exhibit substantial amounts of heterogeneity. The slight differences in the models can be attributed to differences in the datasets used to construct the models.

A prominent low velocity anomaly is observed beneath the MBL block (Anomaly A; Figs. 3, 4) in both the P- and S-wave models. The maximum V<sub>p</sub> amplitude is  $-1.0\%$  in the center and western portions of Anomaly A. The maximum V<sub>s</sub> amplitude of Anomaly A

is  $-2.0\%$  in the center of the model with lower amplitudes of  $\leq -1.0\%$  elsewhere. For both the P- and S-wave models, the vertical extent of Anomaly A can be seen in cross-section a-a' (Fig. 5a), located along the strike of the seismic transect array. With increasing depth, the P-wave anomaly widens and the amplitude increases. In cross-section a-a', Anomaly A is wider ( $\sim 500$  km) in the S-wave model compared to the P-wave model ( $\sim 400$  km). In cross-section b-b' (Fig. 5b), Anomaly A extends to  $\sim 400$  km depth in both the P- and S-wave models and is wider ( $\sim 600$  km W-E) in the S-wave model compared to the P-wave model ( $\sim 450$  km W-E).

Anomaly B, also a region of low velocity ( $\sim -0.5\% V_p$ ,  $\sim -1.5\% V_s$ ), is predominantly located in the central portion of the TIE block and extends towards TG (Figs. 3, 4). The western portion of Anomaly B is located beneath the mouth of TG, with the eastern portion extending beneath the PIG and TIE Neogene volcanic fields. In the P-wave model, Anomaly B extends  $\sim 600$  km (E-W) in length, with increasing width (N-S) from west ( $\sim 200$  km) to east ( $\sim 400$  km) (Fig. 3). In the S-wave model, Anomaly B measures  $\sim 500$  km in length and exhibits variable width (N-S) from west to east (Fig. 4). Cross-section b-b' shows the vertical extent of Anomaly B (Fig. 5b).

Anomaly C is a high velocity anomaly that covers much of the central WARS, with maximum amplitudes located south of PIG (Figs. 3, 4). In the P-wave model, Anomaly C has an irregular shape that is  $\sim 450$  km wide (N-S) and  $\sim 600$  km long (W-E) with an amplitude of  $\leq 0.8\%$ . In the S-wave model, Anomaly C has an amplitude of  $1.5\%$  and is more spatially confined than in the P-wave anomaly. Anomaly C also has an irregular shape in the S-wave model, spanning  $\sim 400$  km N-S and  $\sim 600$  km E-W. The vertical extent of Anomaly C is shown in cross-sections c-c' and d-d' (Fig. 5c-d). In cross section c-c', both the P- and S-wave anomalies narrow with increasing depth. In cross-section d-d' of the P-wave model, Anomaly C is  $\sim 600$  km wide from 100–400 km depth. Whereas,

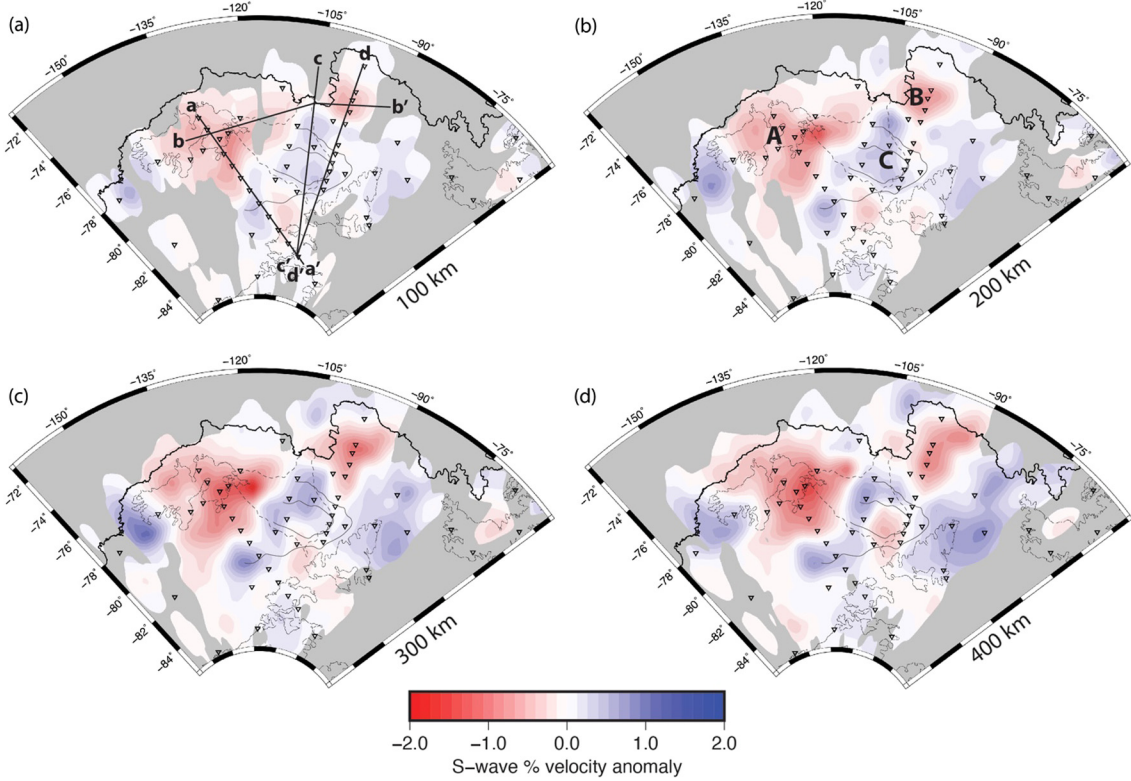


**Fig. 4.** a-d) Depth slices through the S-wave model at 100 km increments. Station locations are marked with triangles. Black lines segments in (a) delineate cross-section locations (a-a', b-b', c-c', d-d'), shown in Fig. 5. The thin, solid black lines contour the 2000 m bedrock elevation. Anomalies A-C, labeled in (b), are discussed in the text.

in the S-wave model, Anomaly C is rather confined along cross-section c-c', being 200 km wide from 100–325 km depth.

## 7. Resolution tests

### 7.1. Checkerboard tests

Model resolution was assessed using a series of synthetic checkerboard tests (Figs. 6, 7, 8, Supp. Figs. 3, 4, 5). The checkerboard tests were composed of Gaussian-tapered spheres with alternating peak amplitudes of  $\pm 5\%$  and radii of 50 km and 100 km placed at 100, 200, 300, and 400 km depth (Supp. Fig. 3). For these tests, synthetic travel times were calculated by ray tracing through the models. Consistent with the standard errors associated with the P- and S-wave arrival time estimates, noise was added to the synthetic travel times as a Gaussian residual time error with a standard deviation of 0.04 s and 0.1 s for P-waves and S-waves, respectively. The synthetic data were then inverted to determine which parts of the model domain show the best recovery. In both the P- and S-wave models, checker recovery depends on the azimuthal source distribution (Fig. 2) and the regularization (i.e., smoothing and flattening) used in the inversion.

For the 100 km radius spheres in the P-wave model, the majority of checkers are recovered with roughly 20–30% of the initial amplitude at every depth increment (Fig. 6). Compared to the 100 km spheres, the 50 km spheres in the P-wave model exhibit lower amplitude recovery (Supp. Fig. 4). Although lacking in amplitude recovery, the majority of checkers are recovered for the 50 km radius spheres in the P-wave model, with the best checker recovery in the WARS, MBL, and PIG regions (Supp. Fig. 4).

Compared to the P-wave model, the checker recovery is not as good in the S-wave model. For the 100 km radius spheres in the S-wave model, a majority of checkers are recovered between 200–400 km depth with  $\sim 15$ –25% of the initial amplitudes (Fig. 7).

For 100–200 km depth, the checker recovery is best in the WARS, MBL, TG, and PIG regions (Fig. 7). For the 50 km radius spheres in the S-wave model, the only notable checker recovery occurs at 200–300 km depth in the WARS and PIG regions (Supp. Fig. 5).

Cross-sections a-a', b-b', c-c', and d-d' transect regions of particular interest in central WANT. To evaluate vertical resolution in our models, the cross sections show profiles of 100 km radius input spheres centered at 200 km depth (Fig. 8). The sides of the spheres are well imaged, indicating that anomalies on the order of 200 km wide can be spatially resolved. However, the cross-sections exhibit  $>150$  km of vertical smearing from the initial input sphere, with peak amplitudes imaged at  $\sim 190$  km depth rather than the input depth of 100 km (Fig. 8). Therefore, the vertical resolution of the P- and S-wave models is more limited, as is common in body wave tomography due to the vertical nature of the ray paths. Given the limited vertical resolution, it is difficult to constrain the depth extent of the imaged anomalies; however, the anomalies likely reside at shallower depths than shown in the models (i.e. the anomalies are smeared downward).

### 7.2. Tabular body tests

To further assess resolution in the P-wave model, we generated a number of tabular body models for cross-sections a-a' and d-d' (Fig. 9a, d). A tabular body is a synthetic velocity structure, similar to the spheres used in the checkerboard tests, with specified amplitude, length, width, and depth derived to be consistent with our final model (Fig. 5; Fig. 9c, f). Similar to the checkerboard tests, we created and inverted synthetic travel times to evaluate structure recoverability using the same parameterization as in our actual model. For the most part, the recovered amplitudes of the tabular body velocity anomalies range from  $\sim 10$ –20% of the synthetic input (Fig. 9b, e). One notable difference between the pattern in the recovered tabular body test and the final model occurs beneath MBL in profile a-a'. The recovered low Vp anomaly beneath

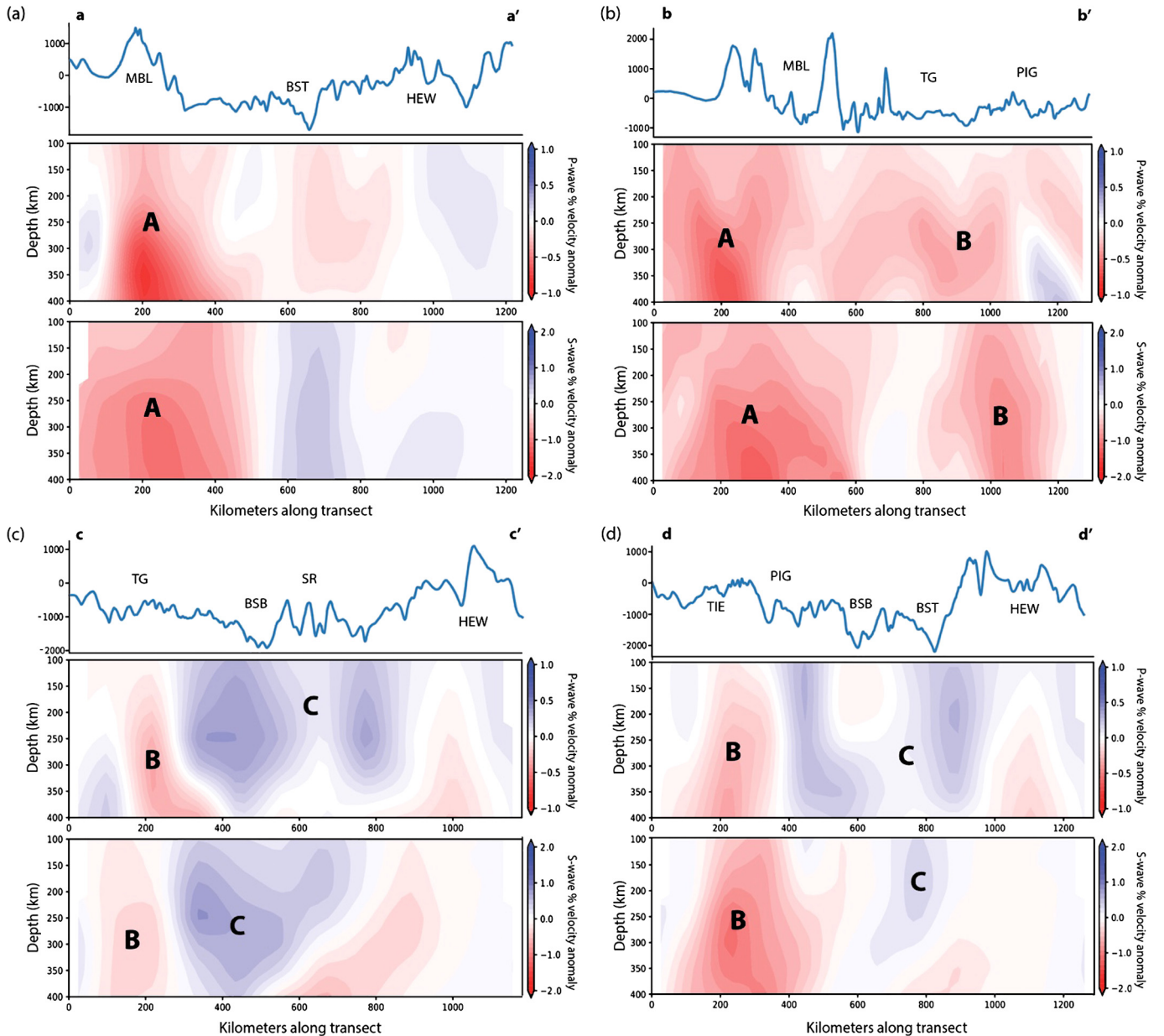


**Fig. 5.** a-d) Cross sections a-a', b-b', c-c', and d-d' through the P- and S-wave tomography models, with bed elevation profiles (from BEDMAP2; Fretwell et al., 2013). Geographic features have same abbreviations as in Fig. 1.

MBL does not extend as deep as Anomaly A in our model (Supp. Fig. 6), indicating that the input synthetic anomaly beneath MBL was either too weak or too shallow. Consequently, the low velocity structure beneath MBL could extend deeper than 225 km, the maximum depth of the input tabular body. After extending the maximum depth of the input tabular body beneath MBL to 400 km (Fig. 9a), the recovered anomaly exhibits comparable structure to Anomaly A in our model (Fig. 9b-c).

## 8. Discussion

Our models reveal significant heterogeneity in upper mantle structure throughout central WANT, including velocity anomalies not clearly imaged in prior studies. The key upper mantle anomalies imaged in this study include low velocities beneath MBL (Anomaly A), high velocities throughout much of the central WARS (Anomaly C), low velocities beneath the mouth of the TG, PIG, and TIE Neogene volcanic fields (Anomaly B), and variable structure in the HEW block (Figs. 3, 4, 5). With the exception of Anomaly A be-

neath MBL (Figs. 3, 4, 5a-b), the vertical resolution tests (Figs. 8, 9) indicate that the anomalies present in our models primarily originate from heterogeneous structure in the uppermost mantle, at depths between the Moho and 150–200 km.

At upper mantle depths, seismic velocities are primarily influenced by temperature variations (e.g., Goes et al., 2000; Faul and Jackson, 2005). In this study, we estimate thermal anomalies from the S-wave velocity anomalies, given that S-waves are more sensitive to temperature variations compared to P-waves. The velocity anomaly magnitudes are underestimated due to the regularization used in the inversion; therefore, when calculating thermal anomalies, we scale the Vs anomaly magnitudes based on the ~25% Vs amplitude recovery in the checkerboard resolution tests. Following the temperature-velocity relationship in Goes et al. (2000) that states a 100 K temperature anomaly corresponds to a 0.7–4.5% Vs anomaly, we calculate minimum thermal anomaly estimates assuming that a 4.5% Vs anomaly is associated with a 100 K temperature anomaly.

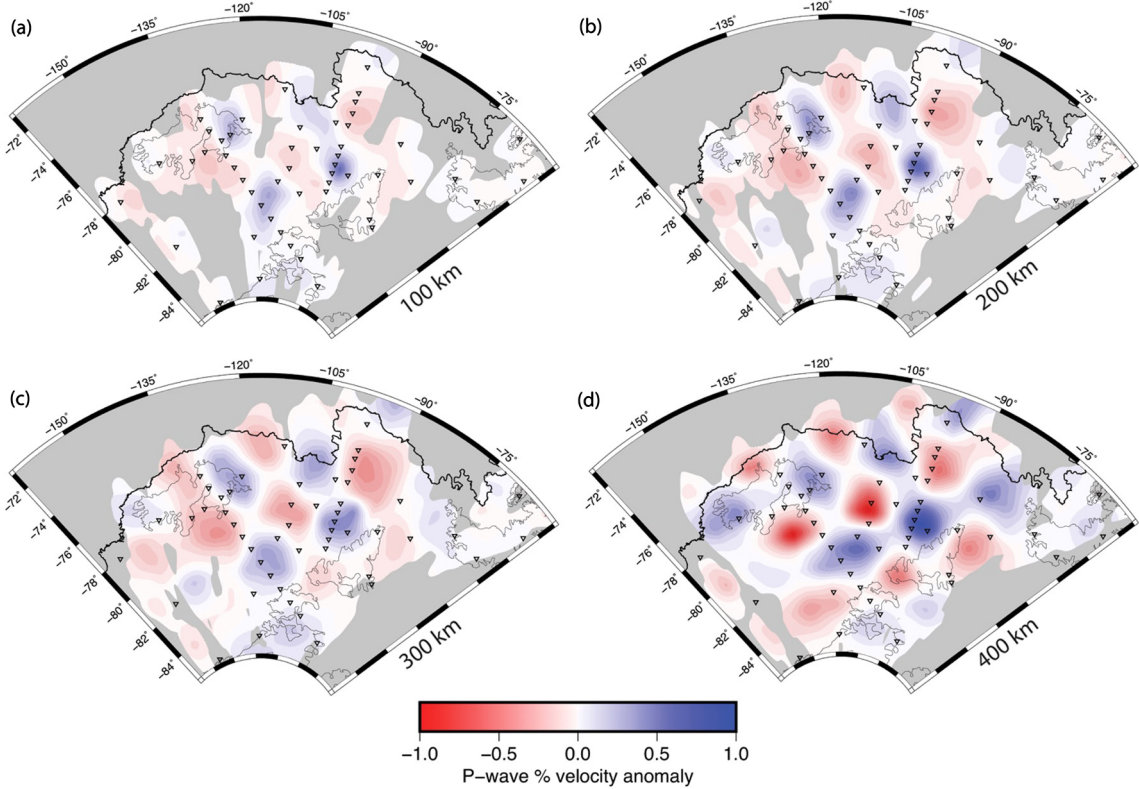


**Fig. 6.** a-d) Recovered P-wave model structure from input synthetic model (Supp. Fig. 3a) with 100 km radius Gaussian tapered spheres centered at 100 km depth increments.

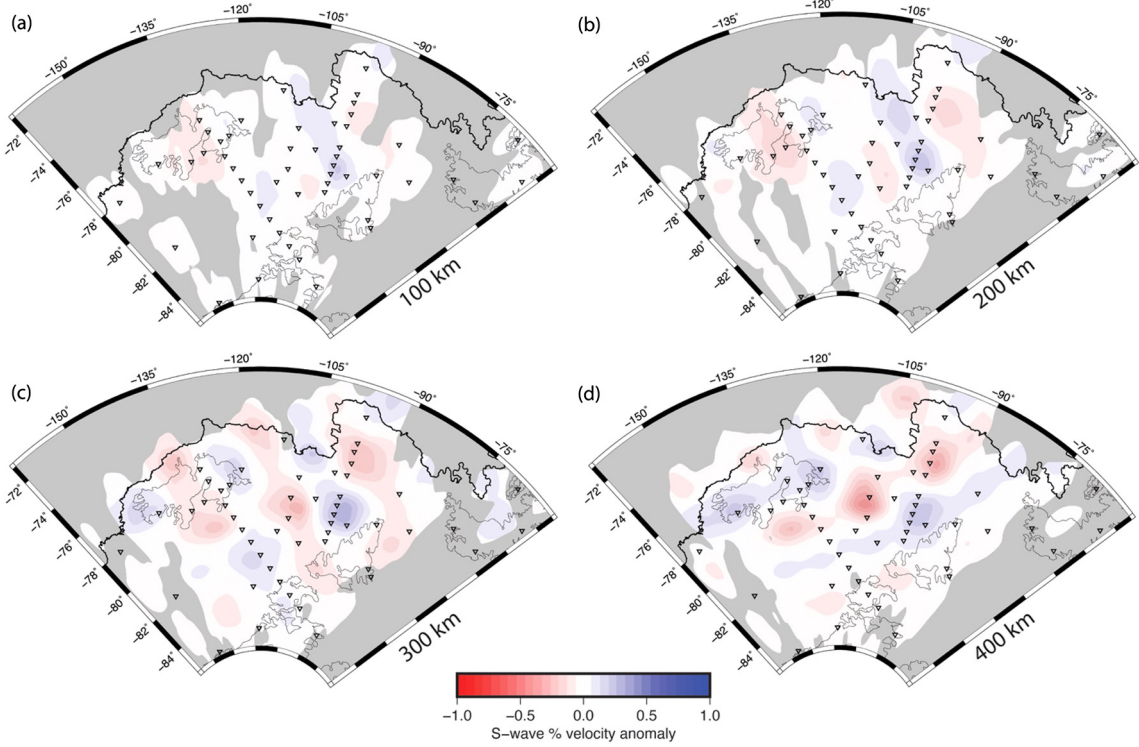


**Fig. 7.** a-d) Recovered S-wave model structure from input synthetic model (Supp. Fig. 3a) with 100 km radius Gaussian tapered spheres centered at 100 km depth increments.

### 8.1. Marie Byrd Land

The lowest velocities in both the P- and S-wave models are beneath MBL (Anomaly A) (Figs. 3, 4, 5a-b). The spatial extent of the anomaly correlates well with uplifted regions throughout

MBL, with the maximum amplitude located in the center of MBL beneath areas of highest elevation (Fig. 5a-b). The location and amplitude of Anomaly A, after the ~25% amplitude recovery correction, is similar to the low velocity anomaly imaged beneath MBL in several other studies (Hansen et al., 2014; Lloyd et al., 2015;

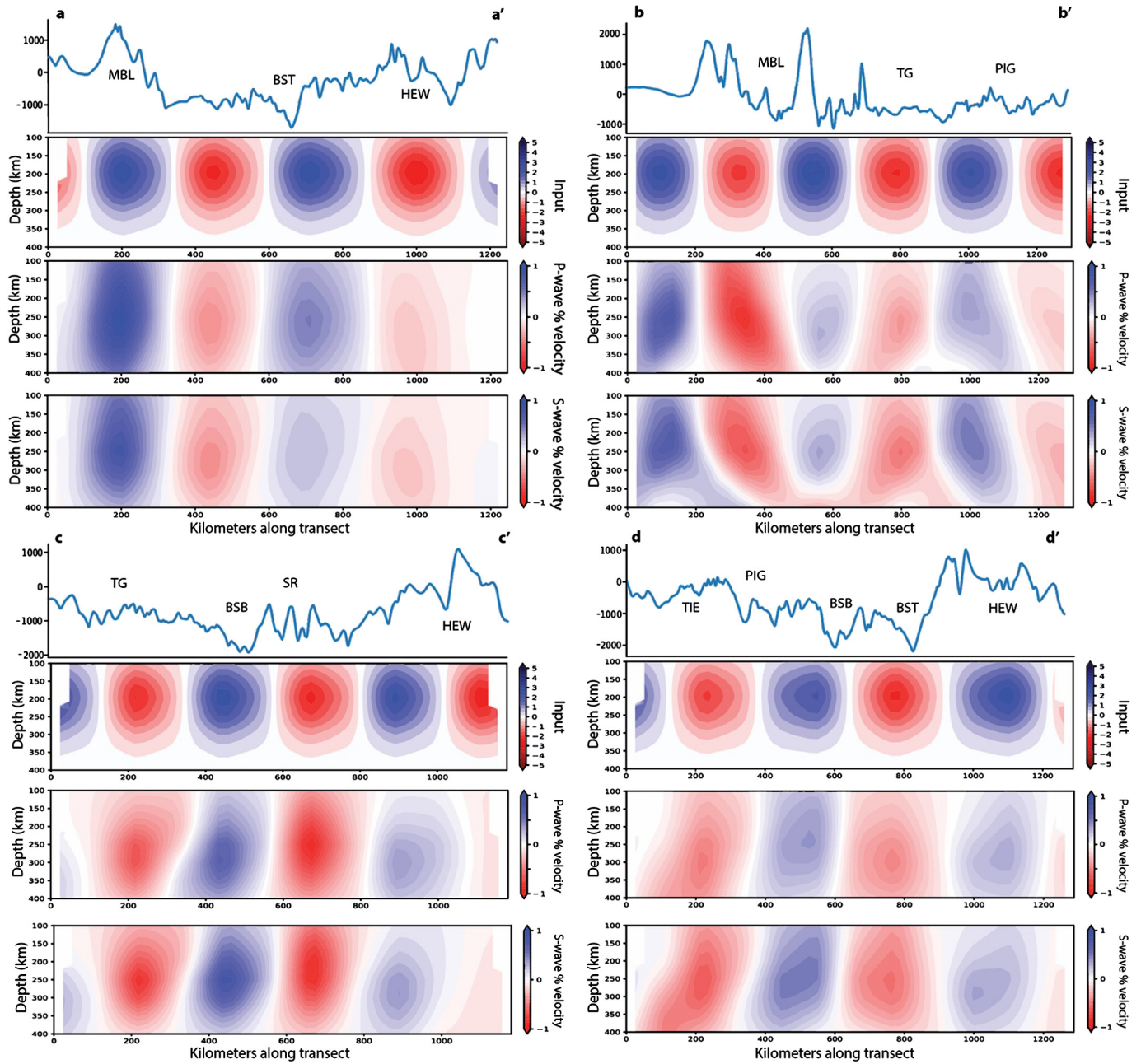


**Fig. 8.** Cross sections a-a', b-b', c-c', and d-d' (Figs. 3a, 4a) showing 100 km radius sphere input model on the upper panel, recovered P-model on middle panel, and recovered S-model on bottom panel. Geographic features have same abbreviations as in Fig. 1.

Heeszel et al., 2016; Shen et al., 2018; White-Gaynor et al., 2019; O'Donnell et al., 2019; Lloyd et al., 2019). The low velocities imaged in this study are consistent with the presence of a mantle plume beneath MBL, as suggested by many studies (e.g., Weaver et al., 1994; LeMasurier and Landis, 1996; Panter et al., 1997; Hansen et al., 2014; Emry et al., 2015; Lloyd et al., 2019). Although we cannot tightly constrain the depth extent of Anomaly A given the limited vertical resolution in our models, the tabular body tests indicate that Anomaly A may extend to ~400 km depth.

After scaling the  $-2.0\%$  S-wave anomaly beneath the center of MBL to  $-8.0\%$  Vs, we calculate an upper mantle thermal anomaly of  $\sim 175$  K (Fig. 4). This minimum thermal anomaly estimate is comparable to both the Lloyd et al. (2015) estimate of  $\sim 150$  K and the Shen et al. (2018) estimate of 200–300 K. The amplitude of Anomaly A is lower in the eastern portion of MBL, indicative of at least a  $\sim 70$  K thermal anomaly (Fig. 4). The estimated minimum

thermal anomaly of  $\sim 70$ – $175$  K in the upper mantle provides sufficient buoyancy to support the topography of MBL, as shown by Chaput et al. (2014). Given the ongoing volcanism in MBL, it is possible that the thermal estimates may be affected by partial melt (O'Donnell et al., 2017).

#### 8.2. Pine Island Glacier, Thwaites Glacier, and TIE Neogene volcanic fields

Low velocities (Anomaly B) are imaged beneath the PIG, TG, Hudson Mountains, and Jones Mountains (Figs. 3, 4, 5b-d). Several other studies (Heeszel et al., 2016; Shen et al., 2018; O'Donnell et al., 2019; Lloyd et al., 2019) also image low velocities in this region of WANT, but across a wider area. In comparison to previous studies, the higher spatial resolution of our model suggests that Anomaly B is confined to the mouth of the TG in the west and ex-

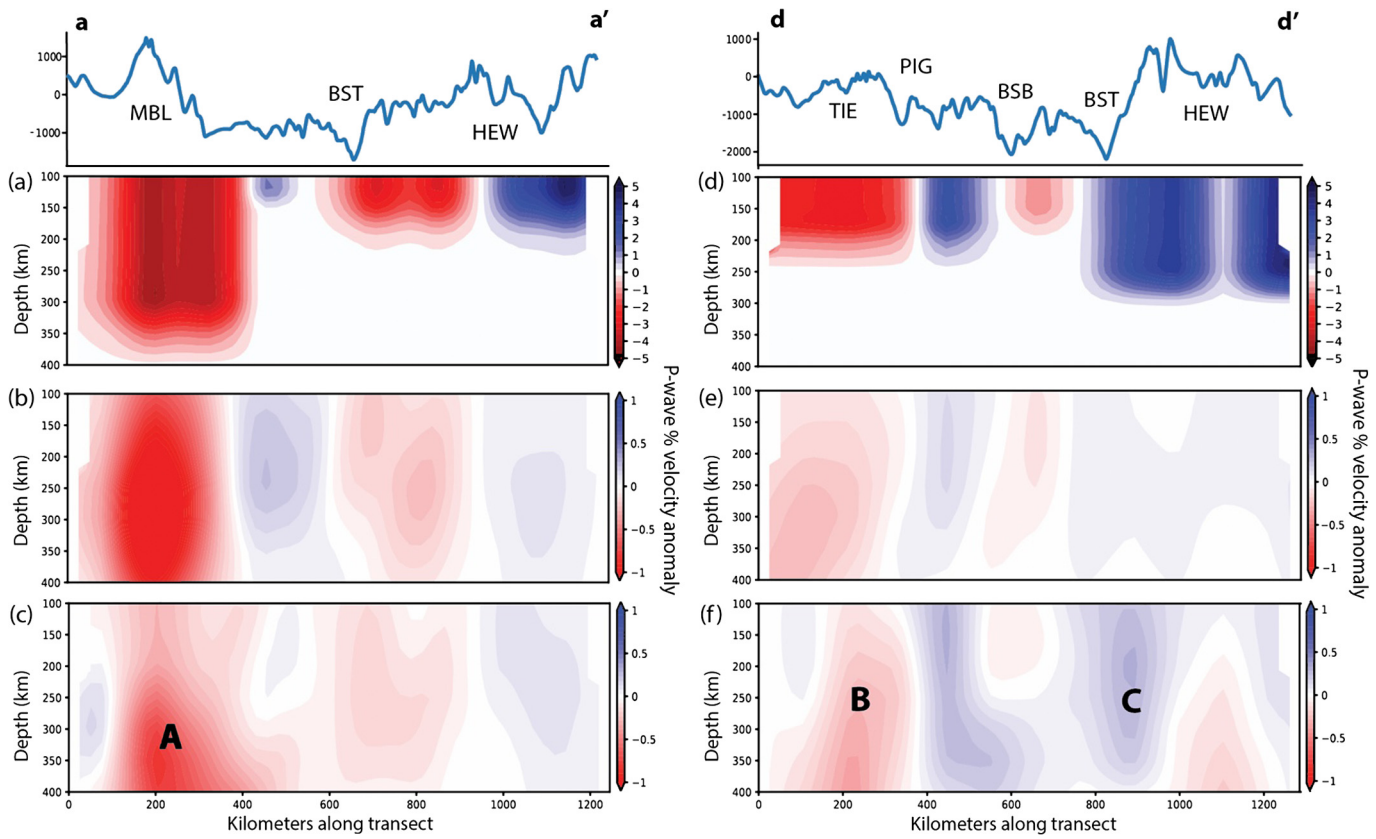


**Fig. 9.** a) Cross section a-a' (Figs. 3a, 4a) with tabular body synthetic input and (b) corresponding recovered P-model anomalies. The low velocity anomaly beneath MBL extends to  $\sim 350$  km depth. c) Cross-section a-a' through the actual P-wave model for comparison. d) Cross section d-d' (Figs. 3a, 4a) with tabular body synthetic input and (e) corresponding recovered P-model anomalies. f) Cross section d-d' through the actual P-wave model for comparison. Geographic features have same abbreviations as in Fig. 1.

tends east towards PIG and the TIE Neogene volcanic fields. After correction for the  $\sim 25\%$  Vs amplitude recovery in the checkerboard resolution tests, the  $-1.2\%$  and  $-0.5\%$  Vs anomalies beneath PIG and TG, respectively, correspond to  $-4.8\%$  and  $-2.0\%$  Vs anomalies. The  $-4.8\%$  Vs anomaly beneath PIG indicates a minimum thermal perturbation of  $\sim 100$  K (Fig. 4), and the  $-2.0\%$  Vs anomaly beneath TG indicates a minimum thermal perturbation of  $\sim 45$  K (Fig. 4). The presence of a thermal anomaly beneath PIG is supported by an aerogravity study, where Jordan et al. (2010) found evidence for Cenozoic mafic intrusions and narrow-mode rifting beneath PIG.

The low velocities imaged in this study are consistent with evidence of both Cenozoic extension (Jordan et al., 2010) and Neogene volcanic activity in the TIE block (Rowley et al., 1990). We find that Anomaly B extends across the mouth of TG and may connect to Anomaly A beneath MBL (Figs. 3, 4, 5b). The possible connection of Anomaly A and B indicates that warm plume material originating in MBL may be flowing east beneath the mouth of the TG, PIG, and TIE Neogene volcanic fields at upper mantle depths. Thus, Anomaly B may result both from Cenozoic extension in the TIE block and warm mantle material from the MBL plume.

### 8.3. West Antarctica Rift System

Generally higher velocities (Anomaly C) are imaged through much of the central WARS including the BSB, Sinuous Ridge, and portions of the BST (Figs. 3, 4, 5c-d). Lloyd et al. (2015) also imaged high velocity anomalies ( $1.8\% V_p$ ;  $3.5\% V_s$ ) along much of the seismic transect array, consistent with our models. O'Donnell et al. (2019), Shen et al. (2018), and Heeszel et al. (2016) show regions of slightly faster upper mantle ( $V_s > 4.3$  km/s) in approximately

the same location of Anomaly C, indicating broad consistency between body and surface wave models.

Narrow ( $\sim 120$  km wide) low velocity anomalies ( $-0.4\% V_p$  and  $-0.5\% V_s$ ) beneath sections of the BST are also imaged in our models (Figs. 3, 4, 5c-d). The low velocities beneath the BST lie mainly along the seismic transect array. Lloyd et al. (2015) also imaged low velocities beneath the BST along the seismic transect array, yet the improved resolution in our models indicate the low velocity anomaly may extend from the seismic transect array towards the Sinuous Ridge (Figs. 3, 4, 5c-d). In addition to the low velocity anomaly imaged along the seismic transect array, we imaged a spatially confined ( $\sim 100$  wide E-W,  $\sim 175$  long N-S) low velocity anomaly beneath the BST at the seismic mini array (Figs. 3, 4, 5c-d).

After correction for the  $\sim 25\%$  Vs amplitude recovery, the higher S-wave velocities ( $\sim 5.6\%$ ) beneath the BSB, Sinuous Ridge and portions of the BST indicate  $\sim 125$  K cooler upper mantle compared to the average WARS upper mantle (Figs. 4, 5c-d). And, after being scaled for Vs amplitude recovery, the lower S-wave velocities ( $-2.0\%$ ) beneath the BST correspond to  $\sim 45$  K warmer upper mantle temperatures compared to the average WARS upper mantle (Figs. 4, 5c-d), resulting in a  $\sim 170$  K minimum difference in upper mantle temperatures beneath the central WARS. Low velocities imaged beneath portions of the BST agree well with the presence of thermally altered lithosphere from localized Cenozoic rifting (Figs. 3, 4, 5c-d), as suggested by Lloyd et al. (2015).

The higher upper mantle velocities suggest that the lithosphere beneath much of the WARS, including the BSB, Sinuous Ridge, and portions of the BST, has not been perturbed since the late Cretaceous to early Cenozoic rifting that formed the WARS (Figs. 3, 4, 5c-d). This interpretation is in agreement with a magnetotell-

luric study across the BSB, where high resistivity structure (2000 to 3000 Ohm) was modeled to depths of 100 km, indicating that the lithosphere has not been recently modified (Wannamaker et al., 1996). The relatively fast seismic velocities imaged in this study contrast with the proposed presence of widespread subglacial Cenozoic volcanoes in the WARS based on morphometric analysis of ice-bed topography (van Wyck de Vries et al., 2017). Because P- and S-wave velocities are typically slower beneath regions of active volcanism, it is unlikely that the topographic features identified by van Wyck de Vries et al. (2017) are recently active subglacial volcanoes.

#### 8.4. Haag-Ellsworth Whitmore Mountains crustal block

In our models, variable velocity structure is evident within the HEW crustal block. High velocity anomalies (0.5%  $V_p$  and 0.8%  $V_s$ ) are imaged in the northern and southern portions of the HEW block, while a low velocity anomaly ( $-0.2\%$   $V_p$ ,  $-0.3\%$   $V_s$ ) is imaged in the central portion (Figs. 3, 4, 5). Lloyd et al. (2015) also imaged a relatively high velocity anomaly in the southern portion of the HEW block. O'Donnell et al. (2019) and Shen et al. (2018) imaged low velocities throughout the HEW block. In contrast to the regionally variable velocity structure imaged in our models, Lloyd et al. (2019) imaged near-average mantle velocities throughout the HEW block.

The low velocity anomaly imaged in the central portion of the HEW block indicates a slightly warmer upper mantle (Figs. 3, 4, 5a), consistent with possible lithospheric foundering as suggested by Shen et al. (2018). Although the HEW block has thicker crust compared to other WANT crustal blocks (Shen et al., 2018), isostatic compensation calculations indicate that the crust is too thin to explain present elevations in the HEW block (Chaput et al., 2014). The warm upper mantle imaged could act as a mantle compensation mechanism, thermally supporting present elevations in the HEW block.

#### 8.5. Surface heat flow and viscosity implications

Geothermal heat flux can impact ice sheet stability significantly (e.g., Seroussi et al., 2017), and the West Antarctic Ice Sheet may be particularly vulnerable to collapse due to possibly elevated heat flow in WANT (e.g., Fisher et al., 2015). However, only a few heat flux measurements have been made in WANT and indicate notable variability, ranging from  $69 \text{ mW m}^{-2}$  at Siple Dome (Engelhardt, 2004) to  $200 \text{ mW m}^{-2}$  beneath portions of the TG catchment (Schroeder et al., 2014). Based on similarities in crustal structure and rift timing with the Cretaceous Newfoundland-Iberia passive margins, Ramirez et al. (2016) argued that heat flow values of  $40\text{--}65 \text{ mW m}^{-2}$  are reasonable for the Central WARS and suggested that heat flow anomalies related to the Cretaceous rifting may have dissipated. Using a Bayesian method to estimate heat flow by comparing the seismic structure of Antarctica to the continental United States, Shen et al. (2020) estimated that heat flow in the WARS ranges from about  $60\text{--}85 \text{ mW m}^{-2}$ , with the lowest values in the central WARS. High velocities imaged beneath much of the WARS in our models support studies arguing that heat flow is not elevated in much of the WARS (e.g., Ramirez et al., 2016; Shen et al., 2020).

In WANT,  $\pm 100 \text{ K}$  temperature variations in the upper mantle can result in viscosity changes of up to two orders of magnitude (O'Donnell et al., 2017). Therefore, the heterogenous upper mantle velocity structure imaged in this study, corresponding to temperature variations of  $100 \text{ K}$  or more over distances of less than 100 km, suggests significant lateral variability in upper mantle viscosity throughout central West Antarctica. Of note, the thermal anomaly located beneath PIG and the mouth of TG is consistent

with GPS uplift rates indicating the presence of thin lithosphere (50–60 km thick) and warm, low viscosity asthenosphere that are facilitating the rapid uplift (41 mm/year) from glacial isostatic adjustment (GIA) (Barletta et al., 2018). In contrast to the low velocity anomaly along the Amundsen Coast beneath PIG and the mouth of TG, there is a prominent transition to higher velocities in the interior of TG (Figs. 3, 4, 5c-d). The higher velocities may be indicative of thicker lithosphere and stiffer upper mantle, which could lead to slower GIA within the interior of TG compared to the mouth of TG. Overall, laterally variable upper mantle viscosity structure has significant implications for the spatial rebound patterns and rates of GIA in central WANT.

#### 9. Summary and conclusions

In this study, data recorded by the POLENET and UKANET seismic networks have been used to generate new P- and S-wave models of upper mantle structure for central WANT. Our models reveal significant heterogeneity in upper mantle structure throughout central WANT and image previously-identified velocity anomalies with improved resolution.

Consistent with previous studies, the low velocity anomaly imaged beneath MBL is interpreted as an upper mantle thermal anomaly, possibly originating from a plume. The low velocities imaged beneath the PIG, the Hudson and Jones Mountains, and the mouth of the TG may indicate that the MBL mantle plume extends east beneath the TIE block. The thermal anomaly beneath PIG and the mouth of TG is consistent with the presence of thin lithosphere and warm asthenosphere, both of which could facilitate rapid GIA uplift. We image a prominent change from the lower velocities at the mouth of TG to higher velocities in the interior of TG, suggesting slower GIA in the interior of TG. Heterogenous structure is imaged beneath the HEW block, including a low velocity anomaly consistent with possible lithospheric foundering in the region. We interpret the high velocity anomalies imaged throughout the central WARS as lithosphere that has not been modified by any tectonic activity since the Mesozoic rifting that formed the WARS. Low velocity anomalies beneath parts of the BST are interpreted as thermally altered areas of localized Cenozoic rifting within the WARS.

The variations in S-wave velocities between regions of lower and higher velocities indicate that upper mantle temperature beneath central WANT could vary by  $100 \text{ K}$  over distances of 100 km or less. Such variation in upper mantle temperature could result in significant lateral variability in upper mantle viscosity throughout central WANT, which could impact glacial isostatic adjustment and thus influence the stability of the West Antarctic Ice Sheet.

#### Declaration of competing interest

The authors declare that they have no known competing financial interests or personal relationships that could have appeared to influence the work reported in this paper.

#### Acknowledgements

This work was supported by the National Science Foundation (NSF) (grants 1142126, 1142518, 1141916, 1148982, 1246416, 1246151, 1249631, 1249602, 1249513, 1246666, 1246712, 1246776, 1247518) and by the Natural Environment Research Council (grants NE/L006065/1, NE/L006294/1, NE/K009958/1). POLENET/ANET seismic instrumentation was provided and supported by the Incorporated Research Institutions for Seismology (IRIS) through the Portable Array Seismic Studies of the Continental Lithosphere (PASSCAL) Instrument Center at New Mexico Tech. UKANET seismic instrumentation was provided and supported by SEIS-UK. We

thank three anonymous reviewers for constructive and helpful reviews.

## Appendix A. Supplementary material

Supplementary material related to this article can be found online at <https://doi.org/10.1016/j.epsl.2020.116437>.

## References

- Accardo, N.J., Wiens, D.A., Hernandez, S., Aster, R.C., Nyblade, A.A., Huerta, A., Anandakrishnan, S., Wilson, T., Heeszel, D.S., Dalziel, I.W.D., 2014. Upper mantle seismic anisotropy beneath the West Antarctic Rift System and surrounding region from shear wave splitting analysis. *Geophys. J. Int.* 198 (1), 414–429. <https://doi.org/10.1093/gji/ggu117>.
- An, M., Wiens, D.A., Zhao, Y., Feng, M., Nyblade, A., Kanao, M., Li, Y., Maggi, A., Lévéque, J.J., 2015. Temperature, lithosphere-asthenosphere boundary, and heat flux beneath the Antarctic Plate inferred from seismic velocities. *J. Geophys. Res.* 120 (12), 8720–8742. <https://doi.org/10.1002/2015JB011917>.
- Barletta, V.R., Bevis, M., Smith, B.E., Wilson, T.J., Brown, A., Bordoni, A., Willis, M., Khan, S.A., Rovira-Navarro, M., Dalziel, I.W., Smalley Jr., R., Kendrick, E., Konfal, S., Caccamise, D.J., Aster, R.C., Nyblade, A.A., Wiens, D.A., 2018. Observed rapid bedrock uplift in Amundsen Sea Embayment promotes ice-sheet stability. *Science* 360 (6395), 1335–1339. <https://doi.org/10.1126/science.aa01447>.
- Behrhardt, J.C., Saltus, R., Damaske, D., McCafferty, A., Finn, C.A., Blankenship, D., Bell, R.E., 1996. Patterns of late Cenozoic volcanic and tectonic activity in the West Antarctic rift system revealed by aeromagnetic surveys. *Tectonics* 15 (3), 660–676. <https://doi.org/10.1029/95TC03500>.
- Chaput, J., Aster, R.C., Huerta, A., Sun, X., Lloyd, A.D., Wiens, D., Nyblade, A.A., Anandakrishnan, S., Winberry, J.P., Wilson, T., 2014. The crustal thickness of West Antarctica. *J. Geophys. Res., Solid Earth* 119 (1), 378–395. <https://doi.org/10.1002/2013jb010642>.
- Corr, H., Vaughan, D., 2008. A recent volcanic eruption beneath the West Antarctic ice sheet. *Nat. Geosci.* 1, 122–125. <https://doi.org/10.1038/ngeo106>.
- Curtis, M.L., 2001. Tectonic history of the Ellsworth Mountains, West Antarctica: reconciling a Gondwana enigma. *Geol. Soc. Am. Bull.* 113 (7), 939–958. [https://doi.org/10.1130/0016-7606\(2001\)113<0939:THOTEM>2.0.CO;2](https://doi.org/10.1130/0016-7606(2001)113<0939:THOTEM>2.0.CO;2).
- Dalziel, I.W.D., 1992. Antarctica: a tale of two supercontinents? *Annu. Rev. Earth Planet. Sci.* 20 (1), 501–526. <https://doi.org/10.1146/annurev.ea.20.050192.002441>.
- Dalziel, I.W.D., Elliott, D.H., 1982. West Antarctica: problem child of Gondwanaland. *Tectonics* 1 (1), 3–19. <https://doi.org/10.1029/tc001i001p00003>.
- Daneshi, S., Morelli, A., 2001. Structure of the upper mantle under the Antarctic Plate from surface wave tomography. *Geophys. Res. Lett.* 28 (23), 4395–4398. <https://doi.org/10.1029/2001gl013431>.
- Donnellan, A., Luyendyk, B.P., 2004. GPS evidence for a coherent Antarctic plate and for postglacial rebound in Marie Byrd Land. *Glob. Planet. Change* 42 (1), 305–311. <https://doi.org/10.1016/j.gloplacha.2004.02.006>.
- Emry, E.L., Nyblade, A.A., Julià, J., Anandakrishnan, S., Aster, R.C., Wiens, D.A., Huerta, A.D., Wilson, T.J., 2015. The mantle transition zone beneath West Antarctica: seismic evidence for hydration and thermal upwellings. *Geochem. Geophys. Geosyst.* 16 (1), 40–58. <https://doi.org/10.1002/2014gc005588>.
- Engelhardt, H., 2004. Ice temperature and high geothermal flux at Siple Dome, West Antarctica, from borehole measurements. *J. Glaciol.* 50 (169), 251–256. <https://doi.org/10.3189/172756504781830105>.
- Faul, U.H., Jackson, I., 2005. The seismological signature of temperature and grain size variations in the upper mantle. *Earth Planet. Sci. Lett.* 234 (1), 119–134. <https://doi.org/10.1016/j.epsl.2005.02.008>.
- Fisher, A.T., Mankoff, K.D., Tulaczyk, S.M., Tyler, S.W., Foley, N., the WISSARD Science Team, 2015. High geothermal heat flux measured below the West Antarctic Ice Sheet. *Sci. Adv.* 1 (6). <https://doi.org/10.1126/sciadv.1500093>.
- Fitzgerald, P.G., 2002. Tectonics and landscape evolution of the Antarctic plate since the breakup of Gondwana, with an emphasis on the West Antarctic Rift System and the Transantarctic Mountains. *Bull. R. Soc. N. Z.* 35, 453–469.
- Fretwell, P., Pritchard, H.D., Vaughan, D.G., Bamber, J.L., Barrand, N.E., Bell, R., Bianchi, C., Bingham, R.G., Blankenship, D.D., Casassa, G., Catania, G., 2013. Bedmap2: improved ice bed, surface and thickness datasets for Antarctica. <https://doi.org/10.5194/tcd-6-4-4305-2012>.
- Goes, S., Govers, R., Vacher, P., 2000. Shallow mantle temperatures under Europe from P and S wave tomography. *J. Geophys. Res.* 105 (B5), 11153–11169. <https://doi.org/10.1029/1999JB900300>.
- Granot, R., Cande, S.C., Stock, J.M., Damaske, D., 2013. Revised Eocene-Oligocene kinematics for the West Antarctic rift system. *Geophys. Res. Lett.* 40, 279–284. <https://doi.org/10.1029/2012GL054181>.
- Hansen, S.E., Graw, J.H., Kenyon, L.M., Nyblade, A.A., Wiens, D.A., Aster, R.C., Huerta, A.D., Anandakrishnan, S., Wilson, T.J., 2014. Imaging the Antarctic mantle using adaptively parameterized P-wave tomography: evidence for heterogeneous structure beneath West Antarctica. *Earth Planet. Sci. Lett.* 408, 66–78. <https://doi.org/10.1016/j.epsl.2014.09.043>.
- Harry, D.L., Anoka, J.L., Jha, S., 2018. Geodynamic models of the West Antarctic Rift System: implications for the mantle thermal state. *Geosphere* 14 (6), 2407–2429. <https://doi.org/10.1130/GES01594.1>.
- Heeszel, D.S., Wiens, D.A., Anandakrishnan, S., Aster, R.C., Dalziel, I.W., Huerta, A.D., Nyblade, A.A., Wilson, T.J., Winberry, J.P., 2016. Upper mantle structure of central and West Antarctica from array analysis of Rayleigh wave phase velocities. *J. Geophys. Res., Solid Earth* 121 (3), 1758–1775. <https://doi.org/10.1002/2015jb021616>.
- Hole, M.J., LeMasurier, W.E., 1994. Tectonic controls on the geochemical composition of Cenozoic, mafic alkaline volcanic rocks from West Antarctica. *Contrib. Mineral. Petrol.* 117 (2), 187–202. <https://doi.org/10.1007/BF00286842>.
- Jordan, T., Ferraccioli, F., Leat, P., 2017. New geophysical compilations link crustal block motion to Jurassic extension and strike-slip faulting in the Weddell Sea Rift System of West Antarctica. *Gondwana Res.* 42, 29–48. <https://doi.org/10.1016/j.gr.2016.09.009>.
- Jordan, T.A., Ferraccioli, F., Vaughan, D.G., Holt, J.W., Corr, H., Blankenship, D.D., Diehl, T.M., 2010. Aerogravity evidence for major crustal thinning under the Pine Island Glacier region (West Antarctica). *Geol. Soc. Am. Bull.* 122 (5–6), 714–726. <https://doi.org/10.1130/B26417.1>.
- LeMasurier, W.E., Landis, C.A., 1996. Mantle-plume activity recorded by low-relief erosion surfaces in West Antarctica and New Zealand. *Geol. Soc. Am. Bull.* 108 (11), 1450–1466. [https://doi.org/10.1130/0016-7606\(1996\)108<1450:MPARBL>2.3.CO;2](https://doi.org/10.1130/0016-7606(1996)108<1450:MPARBL>2.3.CO;2).
- LeMasurier, W.E., Thomson, J.W., 1990. Volcanoes of the Antarctic Plate and Southern Oceans. *American Geophysical Union*.
- Lloyd, A.J., Wiens, D.A., Nyblade, A.A., Anandakrishnan, S., Aster, R.C., Huerta, A.D., Wilson, T.J., Dalziel, I.W., Shore, P.J., Zhao, D., 2015. A seismic transect across West Antarctica: evidence for mantle thermal anomalies beneath the Bentley Subglacial Trench and the Marie Byrd Land Dome. *J. Geophys. Res., Solid Earth* 120 (12), 8439–8460. <https://doi.org/10.1002/2015jb012455>.
- Lloyd, A.J., Wiens, D.A., Zhu, H., Tromp, J., Nyblade, A.A., Aster, R.C., Hansen, S.E., Dalziel, I.W.D., Wilson, T.J., Ivins, E.R., O'Donnell, J.P., 2019. Seismic structure of the Antarctic upper mantle based on adjoint tomography. *J. Geophys. Res., Solid Earth* 124. <https://doi.org/10.1029/2019JB017823>.
- Lough, A.C., Wiens, D.A., Barcheck, C.G., Anandakrishnan, S., Aster, R.C., Blankenship, D.D., Huerta, A.D., Nyblade, A.A., Young, D.A., Wilson, T.J., 2013. Seismic detection of an active subglacial magmatic complex in Marie Byrd Land, Antarctica. *Nat. Geosci.* 6 (12), 1031. <https://doi.org/10.1038/ngeo1992>.
- O'Donnell, J.P., Selway, K., Nyblade, A.A., Brazier, R.A., Wiens, D.A., Anandakrishnan, S., Aster, R.C., Huerta, A.D., Wilson, T.J., Winberry, J.P., 2017. The uppermost mantle seismic velocity and viscosity structure of central West Antarctica. *Earth Planet. Sci. Lett.* 472, 38–49. <https://doi.org/10.1016/j.epsl.2017.05.016>.
- O'Donnell, J.P., Stuart, G.W., Brisbourne, A.M., Selway, K., Yang, Y., Nield, G.A., Whitehouse, P.L., Nyblade, A.A., Wiens, D.A., Aster, R.C., Anandakrishnan, S., Huerta, A.D., Wilson, T., Winberry, J.P., 2019. The uppermost mantle seismic velocity structure of West Antarctica from Rayleigh wave tomography: insights into tectonic structure and geothermal heat flow. *Earth Planet. Sci. Lett.* 522, 219–233. <https://doi.org/10.1016/j.epsl.2019.06.024>.
- Panter, K.S., Kyle, P.R., Smellie, J.L., 1997. Petrogenesis of a phonolite-trachyte succession at Mount Sidley, Marie Byrd Land, Antarctica. *J. Petrol.* 38 (9), 1225–1253. <https://doi.org/10.1093/petroj/38.9.1225>.
- Pattyn, F., Morlighem, M., 2020. The uncertain future of the Antarctic Ice Sheet. *Science* 367, 1331–1335. <https://doi.org/10.1126/science.aaz5487>.
- Powell, E., Gomez, N., Hay, C., Latychev, K., Mitrovica, J.X., 2019. Viscous effects in the solid Earth response to modern Antarctic ice mass flux: implications for geodetic studies of WAIS stability in a warming world. *J. Climate* 33, 443–459. <https://doi.org/10.1175/JCLI-D-19-0479.1>.
- Ramirez, C., Nyblade, A., Hansen, S.E., Wiens, D.A., Anandakrishnan, S., Aster, R.C., Huerta, A.D., Shore, P., Wilson, T., 2016. Crustal and upper-mantle structure beneath ice-covered regions in Antarctica from S-wave receiver functions and implications for heat flow. *Geophys. J. Int.* 204 (3), 1636–1648. <https://doi.org/10.1093/gji/ggv542>.
- Ramirez, C., Nyblade, A., Emry, E.L., Julià, J., Sun, X., Anandakrishnan, S., Wiens, D.A., Aster, R.C., Huerta, A.D., Winberry, P., Wilson, T., 2017. Crustal structure of the Transantarctic Mountains, Ellsworth Mountains and Marie Byrd Land, Antarctica: constraints on shear wave velocities, Poisson's ratios and Moho depths. *Geophys. J. Int.* 211 (3), 1328–1340. <https://doi.org/10.1093/gji/gjx333>.
- Ritzwoller, M.H., Shapiro, N.M., Levshin, A.L., Leahy, G.M., 2001. Crustal and upper mantle structure beneath Antarctica and surrounding oceans. *J. Geophys. Res., Solid Earth* 106 (B12), 30645–30670. <https://doi.org/10.1029/2001JB000179>.
- Roult, G., Rouland, D., Montagner, J.P., 1994. Antarctica II: upper-mantle structure from velocities and anisotropy. *Phys. Earth Planet. Inter.* 84 (1–4), 33–57. [https://doi.org/10.1016/0031-9201\(94\)90033-7](https://doi.org/10.1016/0031-9201(94)90033-7).
- Rowley, P.D., Thomson, J.W., Smellie, J.L., Laudon, T.S., La Prade, K.E., LeMasurier, W.E., 1990. Alexander Island, Palmer Land, and Ellsworth Land. In: LeMasurier, W.E., et al. (Eds.), *Volcanoes of the Antarctic Plate and Southern Oceans*. In: *American Geophysical Union, Antarctic Research Series*, vol. 48, pp. 296–298.
- Schroeder, D.M., Blankenship, D.D., Young, D.A., Quartini, E., 2014. Evidence for elevated and spatially variable geothermal flux beneath the West Antarctic Ice Sheet. *Proc. Natl. Acad. Sci. USA* 111 (25), 9070–9072. <https://doi.org/10.1073/pnas.1405184111>.

- Seroussi, H., Ivins, E.R., Wiens, D.A., Bondzio, J., 2017. Influence of a West Antarctic mantle plume on ice sheet basal conditions. *J. Geophys. Res., Solid Earth* 122, 7127–7155. <https://doi.org/10.1002/2017JB014423>.
- Shen, W., Wiens, D.A., Anandakrishnan, A., Aster, R.C., Gerstoft, P., Bromirski, P., Hansen, S.E., Dalziel, I., Heeszel, D., Huerta, A., Nyblade, A.A., Stephen, R., Wilson, T., Winberry, J.P., 2018. The crust and upper mantle structure of central and West Antarctica from Bayesian inversion of Rayleigh wave and receiver functions. *J. Geophys. Res.* 123. <https://doi.org/10.1029/2017JB015346>.
- Shen, W., Wiens, D., Lloyd, A., Nyblade, A., 2020. A geothermal heat flux map of Antarctica empirically constrained by seismic structure. *Geophys. Res. Lett.* 47. <https://doi.org/10.1029/2020GL086955>.
- Shepherd, A., Gilbert, L., Muir, A.S., Konrad, H., McMillan, M., Slater, T., Briggs, K.H., Sundal, A.V., Hogg, A.E., Engdahl, M.E., 2019. Trends in Antarctic Ice Sheet elevation and mass. *Geophys. Res. Lett.* 46, 8174–8183. <https://doi.org/10.1029/2019GL082182>.
- Siddoway, C.S., 2008. Tectonics of the West Antarctic rift system: new light on the history and dynamics of distributed intracontinental extension. In: Cooper, A., et al. (Eds.), *Antarctica: a Keystone in a Changing World*. National Academy of Sciences, Washington, D.C., pp. 91–114.
- Torsvik, T.H., Gaina, C., Refeld, T.F., 2008. Antarctica and global paleogeography: from Rodinia, through Gondwanaland and Pangea, to the birth of the Southern Ocean and the opening of gateways. In: Cooper, A., et al. (Eds.), *Antarctica: a Keystone in a Changing World*. National Academy of Sciences, Washington, D.C., pp. 125–140.
- VanDecar, J.C., 1991. Upper-Mantle Structure of the Cascadia Subduction Zone from Non-Linear Teleseismic Travel-Time Inversion (Doctoral dissertation).
- VanDecar, J.C., Crosson, R.S., 1990. Determination of teleseismic relative phase arrival times using multi-channel cross-correlation and least squares. *Bull. Seismol. Soc. Am.* 80 (1), 150–169.
- van Wyck de Vries, M., Bingham, R.G., Hein, A.S., 2017. A new volcanic province: an inventory of subglacial volcanoes in West Antarctica. *Geol. Soc. (Lond.) Spec. Publ.* 461 (29), 231–248. <https://doi.org/10.1144/SP461.7>.
- Wannamaker, P.E., Stodd, J.A., Olsen, S.L., 1996. Dormant state of rifting below the Byrd Subglacial Basin, West Antarctica, implied by magnetotelluric (MT) profiling. *Geophys. Res. Lett.* 23 (21), 2983–2986. <https://doi.org/10.1029/96GL02887>.
- Weaver, S.D., Storey, B.C., Pankhurst, R.J., Mukasa, S.B., DiVenere, V.J., Bradshaw, J.D., 1994. Antarctica–New Zealand rifting and Marie Byrd Land lithospheric magmatism linked to ridge subduction and mantle plume activity. *Geology* 22 (9), 811–814. [https://doi.org/10.1130/0091-7613\(1994\)022<0811:ANZRAM>2.3.CO;2](https://doi.org/10.1130/0091-7613(1994)022<0811:ANZRAM>2.3.CO;2).
- White-Gaynor, A.L., Nyblade, A.A., Aster, R.C., Wiens, D.A., Bromirski, P.D., Gerstoft, P., Stephen, R.A., Hansen, S.E., Wilson, T., Dalziel, I.W., Huerta, A.D., Winberry, J.P., Anandakrishnan, S., 2019. Heterogeneous upper mantle structure beneath the Ross Sea Embayment and Marie Byrd Land, West Antarctica, revealed by P-wave tomography. *Earth Planet. Sci. Lett.* 513, 40–50. <https://doi.org/10.1016/j.epsl.2019.02.013>.
- Wilch, T.J., McIntosh, W.C., Dunbar, N.W., 1999. Late Quaternary volcanic activity in Marie Byrd Land: potential 40Ar/39Ar-dated time horizons in West Antarctic ice and marine cores. *Geol. Soc. Am. Bull.* 111 (10), 1563–1580. [https://doi.org/10.1130/0016-7606\(1999\)111<1563:LQVAIM>2.3.CO;2](https://doi.org/10.1130/0016-7606(1999)111<1563:LQVAIM>2.3.CO;2).
- Wilson, T.J., Bevis, M., Konfal, S., Barletta, V., Aster, R., Chaput, J., Heeszel, D., Wiens, D., Anandakrishnan, S., Dalziel, I., Huerta, A., Kendrick, E., Nyblade, A., Winberry, P., Smalley, B., Lloyd, A., 2015. Understanding glacial isostatic adjustment and ice mass change in Antarctica using integrated GPS and seismology observations. In: *EGU General Assembly Conference Abstracts*, vol. 17.
- Winberry, J.P., Anandakrishnan, S., 2003. Seismicity and neotectonics of West Antarctica. *Geophys. Res. Lett.* 30 (18). <https://doi.org/10.1029/2003GL018001>.